# LOW-ORDER ABERRATION SUPPRESSION ON PRIMARY MIRROR OF THE TOGS FOR SATELLITE DOWNLINK

**Ming Liu,[1,2]\* Hongwei Zhao,[1] Guanyu Wen,[2] Xiaolin Li,[3] and Chengwei Zhu[2]**

[1]*School of Mechanical and Aerospace Engineering, Jilin University*
*Changchun 130025, China*

[2]*Changchun Observatory, National Astronomical Observatories, CAS*
*Changchun 130117, China*

[3]*Hunan Laguerre Electronic Technology Co. Ltd*
*Hunan 410000, China*

\*Corresponding author e-mail:   lium @ cho.ac.cn

### Abstract

There is a growing interest in the development of transportable optical ground station (TOGS) as an important component of laser communication network. The object of this paper is a TOGS designed for optical LEO satellite downlink as well as for long-distance aircraft downlink. A composite gravity compensation mount is proposed to simplify and efficiently suppress the low-order aberrations of an 800 mm aperture primary mirror with variable orientation of the optical antenna of a TOGS as it changes pointing. In this study, first we describe the composition of the TOGS and the utility of each part. Second, taking the minimization of the primary mirror deformation as the optimization objective, we employ the particle swarm optimization algorithm to find the optima of several key structural parameters by Isight software. Next, the annular Zernike polynomials are adopted to fit the wavefront error over the entire surface of the primary mirror for describing low-order aberrations, proving that the composite mount effectively suppresses the wavefront error to smaller than $\lambda/27$, as the elevation angle changes from the horizontal to the vertical one. Finally, the ZYGO interferometer wavefront detections show that, after eliminating fabrication imperfections, the RMS of the wavefront error over the entire surface of the mirrors for horizontal and vertical axes, due to deformation, are $0.04\lambda$ and $0.035\lambda$, respectively. Compared to the results of the fitted wavefront error, the relative errors are 9.5% and 8.1%. The results show the validity and feasibility of the optimized composite mount and the wavefront fitting method, which can prove its reference significance for the budget and allocation of the systematic wavefront error in meter-scale optical antenna of the TOGS for satellite downlink.

**Keywords:** laser communication, low-order aberration suppression, optomechanics, annular Zernike polynomials, wavefront error measurements.

## 1.   Introduction

There is a growing interest in the development of transportable optical ground station (TOGS) as an important component of laser communication network [1]. As TOGSs for satellite downlink applications may be placed and operated at fixed locations around the globe, especially applications that require the transmission of imagery to a specific location need TOGS, which can be placed at changing locations.

TOGS generally features a Cassegrain-type telescope serving as an optical antenna for tracking and receiving, and different functions can be achieved by connecting different receiving terminals. German Aerospace Center (DLR) developed a TOGS to enable near-real-time data transfer from Earth-observing satellites and aircrafts [2]. The TOGS was first tested as a part of DLR's VABENE Project, in which a 1 Gbps link was established between TOGS and a Dornier aircraft [3]. Tesat Space Company demonstrated coherent inter-satellite laser communications, and a modified version of the TOGS was placed at ESA's Tenerife facility to demonstrate space-to-ground coherent communications [4].

In satellite laser communication, a larger optical antenna aperture of the TOGS is required to increase the power margin and inhibit atmospheric turbulence [5]. However, a large mirror is severely deformed by gravity, and the deviation over the mirror surface directly affects communication quality. Therefore, in order to maintain the desired mirror surface during laser communication, a support structure with aberration suppression on the mirror is essential. The TOGS, studied in this paper, is contained in a carrier vehicle and equipped with an 80 cm aperture optical antenna in Ritchey–Chrétien–Cassegrain configuration for satellite and aircraft downlink. The mercury tube mount is an approximation to the ideal flotation mount to support the mirror by radially directed compressive forces of variable magnitude. Drawing on the advantage of the mercury tube mount, in this paper, we present a composite gravity-compensation mount to suppress the low-order aberration of the primary mirror with variable orientation.

## 2.    Cassegrain Antenna of the TOGS

In this study, we focus on the TOGS with an 800 mm aperture optical antenna, which serves as a vital mobile node in the laser communications network. The TOGS, mounted on a carrier vehicle, consists of an optical antenna in the Ritchey–Chrétien–Cassegrain (R-C) configuration, a coarse tracking lens, a beacon laser emission lens, an acquisition, tracking, and pointing subsystem (ATR), and a two-axes servo turntable; see Fig. 1.

The Cassegrain antenna is used to collect energy and restrict beam spread and block ambient light, so the optical antenna with good optical performance can ensure a high laser power gain. The Ritchey–Chrétien configuration, in which both the primary and secondary mirrors are hyperboloid reflectors, is adopted by the optical antenna and is referred to as R-C system. The Cassegrain antenna is comprised of a primary mirror cell, telescope tube, secondary mirror cell, four-vane spider, and baffle; see Fig. 2. The primary mirror is floated by the composite gravity-compensation mounts, which combine a Hindle axial mount, a mercury tube radial mount, and a hub center mount in the primary mirror cell. The secondary mirror is held by a four-vane spider at the top of the telescope tube. The primary mirror cell, the secondary mirror cell, and the baffle are all linked through the telescope tube. In order to meet the antenna optical design requirement that the root-mean-square (RMS) wavefront error of the exit beam must be smaller than $\lambda/10$ with the optical axis tilted between $+5°$ and $+90°$ in this paper we present a composite mount for large, variable-orientation primary mirror, and its integrated optomechanical analysis.

## 3.    Composite Mount for Large Variable-Orientation Primary Mirror

As the elevation angle of the optical antenna changes, the RMS surface deformation of the primary mirror continuously varies. The composite mount for controlling the distribution of forces acting on the
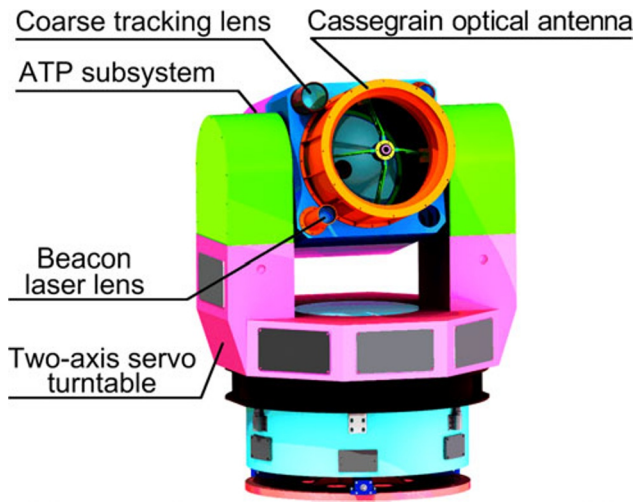
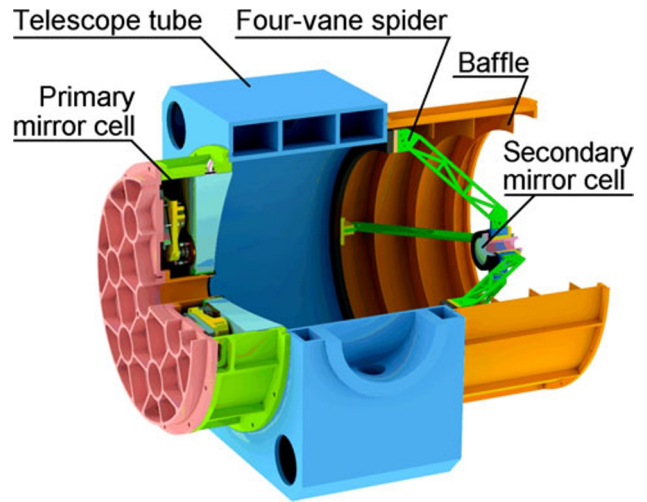**Fig. 1.** The transportable ground station.
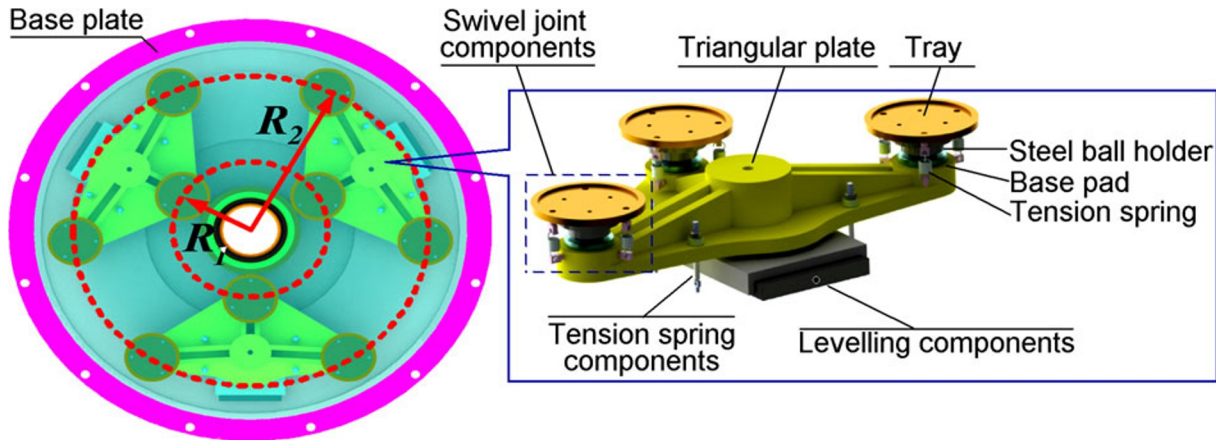


**Fig. 2.** The Cassegrain antenna.



**Fig. 3.** The axial support based on the Hindle mount.

mirror to minimize surface deflection as the mirror orientation changes is described in this section.

## 3.1.   Axial Support Based on Hindle Mount

When the antenna is pointing towards the zenith, the gravitational force of the primary mirror is borne entirely by the axial back support. In a classical literature on mirror flotation systems, Hindle described a nine-point two-ring mounting [6]. To preserve the kinematic nature, the support points on the back of the mirror are grouped in threes and mounted on pivots. They can be arranged on two tiers to form what is called a whiffletree. The axial support consists of swivel joint components, a triangular plate, a base plate, leveling components, and tension spring components; and each swivel joint component consists of a tray, a steel ball, a steel ball holder, three tension springs, and a base pad; see Fig. 3.

Three-point and six-point supports lie on inner and outer circles of radii $R_1$ and $R_2$, respectively; see Fig. 4. Arnold developed an empirical formula, based on Hindle's study, to determine the location of

nine-point supports for the primary mirror with a central aperture [7]; it reads

$$
\begin{cases}
\dfrac{R_1 - r}{D/2 - r} = 0.26 \sim 0.28, \\
\dfrac{R_2 - r}{D/2 - r} = 0.75 \sim 0.76,
\end{cases}
\tag{1}
$$

where $D$ is the diameter of the primary mirror, and $r$ is the radius of the center hole. Then, the calculated values for $R_1$ and $R_2$ are 165 and 330 mm, respectively.

However, the above empirical formula applies to a plate mirror of uniform thickness with a central aperture. Calculations for curved surface mirrors are more complex, as the weight distribution is nonlinear with the radius; thus, the FEA method is frequently used for such cases. First, the finite element model is established. Second, we calculate the response function for each deformation of the mirror caused by $R_1$ and $R_2$ – minimization of the RMS value of the mirror deformation is taken as the optimization objective, the angularly equidistant distributions of $R_1$ and $R_2$ around the radius of equilibrium are taken as the optimization variables, and the fact that each support point bears an equal component of the mirror's gravity is taken



**Fig. 4.** The mapping relationship of mirror deformation.

as the optimization constraint. Finally, we solve the mapping relationship between $R_1$ and $R_2$ and the RMS value of the mirror deformation by Isight software; see Fig. 4.
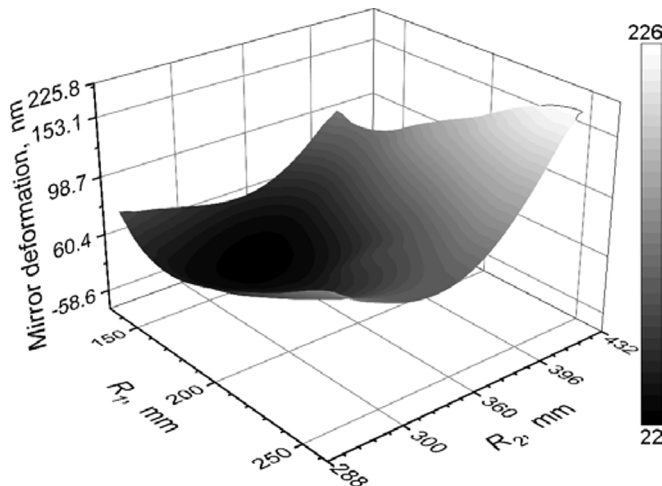
After a series of iterative calculations, we determine the most efficient support positions to be $R_1 = 180.5$ mm and $R_2 = 342$ mm. In Fig. 5, we show the mirror's deformation before and after optimizing its support position. Compared to the empirical formula, the RMS value of the mirror deformation improves from 70.4 to 21.6 nm.
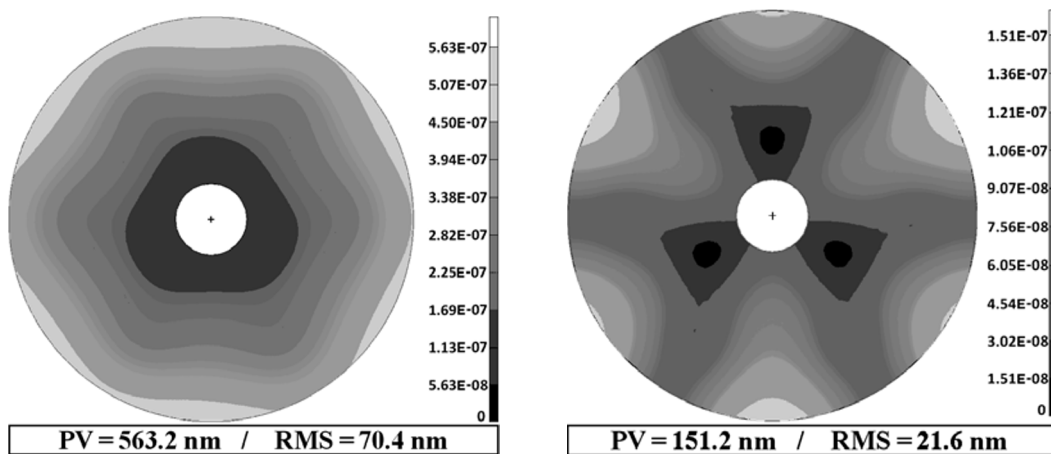


**Fig. 5.** The deformation of the mirror before and after optimizing its support position.

### 3.2.   Radial Composite Support

The mercury tube mount is an approximation to the ideal radial flotation mount to support the mirror's edge by radially directed compressive forces of variable magnitude proportional to mercury column height. However, it is not feasible to the position of the mirror solely by the mercury tube mount. Therefore, a radial composite support composed of the mercury tube mount and central hub mount is employed. The central hub mount not only bears part of the gravity of the primary mirror but also ensures the spatial position of the mirror. Supported by the radial composite support, the forces acting on the primary mirror in the axis-horizontal position are shown in Fig. 6.
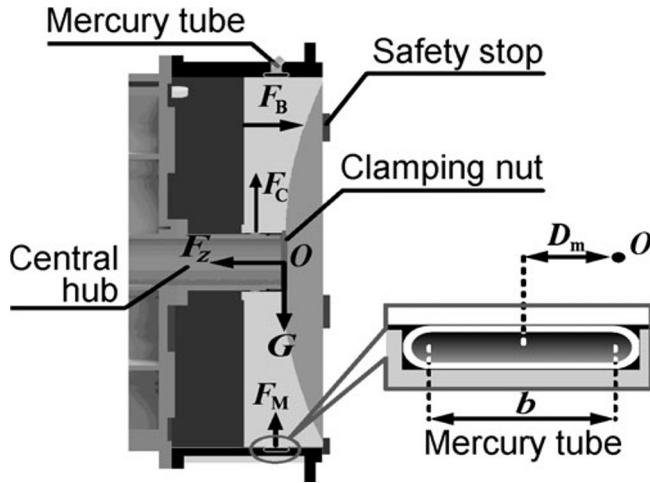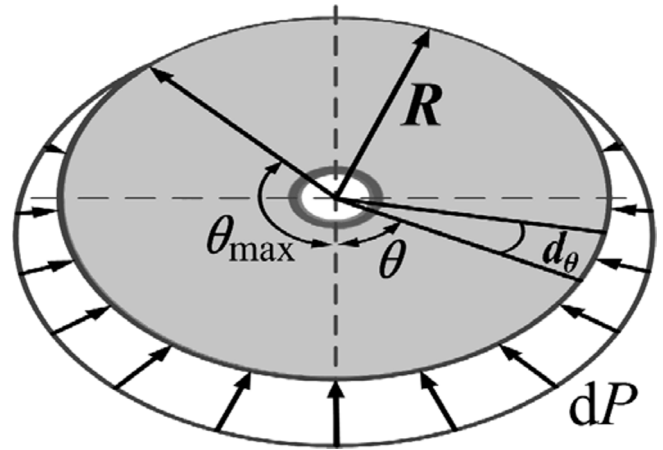


**Fig. 6.** The forces acting on the mirror.          **Fig. 7.** The physical model for the buoyant.

In the above analysis of forces, $F_M$ is the buoyant force by the mercury tube, $F_C$ is the support force by the central hub mount, $G$ is the gravity of the primary mirror, $F_B$ is the support force acting on the back of the mirror by the axial support, and $F_Z$ is the pressure force by the clamping nut. Given that the primary mirror is in a state of force equilibrium, the force equilibrium condition can be expressed as follows:

$$\begin{cases} F_M + F_C + G = 0, \\ \quad F_B + F_Z = 0. \end{cases} \tag{2}$$

Further, in Fig. 7, we illustrate a physical model for the buoyant by the mercury tube. The envelope angle of the mercury tube, wrapping around the primary mirror, is set to $2\theta_{\max}$, and the pressure at an angle $\theta$ in the envelope, being equal to the density multiplied by the height of the mercury column, reads

$$P = \rho g h = \rho g R(\cos\theta - \cos\theta_{\max}), \tag{3}$$

where $h$ is the height of the mercury column, and $\rho$ is the density. Then, the buoyant force generated by the angular element $d\theta$ can be expressed as follows:

$$dF_M = PbRd\theta = R^2\rho g b \left(\cos\theta - \cos\theta_{\max}\right), \tag{4}$$

where $b$ is the width of the mercury tube; see Fig. 6. We determine the buoyant force generated by the whole envelope in the vertical direction as

$$F_M = 2\int_0^{\theta_{\max}} R^2\rho g b (\cos\theta - \cos\theta_{\max})\cos\theta \ d\theta. \tag{5}$$

According to (2)–(5), the finite element model of the primary mirror, which is radially supported by the mercury tube, and the buoyant force of the angular element in the circumferential direction are shown in Fig. 8.

After analyzing the forces acting on the primary mirror and deriving the buoyancy formulation, there are three variable parameters that can be optimized to inhibit the deformation of the mirror surface: first, the envelope angle of the mercury tube, $2\theta_{\max}$; second, the proportion of the primary mirror's gravity borne by the mercury tube, $P_m$; third, the axial distance of the mercury tube from the primary mirror's center of gravity, $D_m$. Note that the width of the mercury tube has already been determined once the envelope angle and the proportion of the primary mirror's gravity borne are determined according to Eqs. (2)–(5). Therefore, it is not regarded as an independent optimization variable parameter.

Similarly, we adopt the Isight software and the FEA method to solve this multivariate optimization problem. The optimization objective is to minimize



**Fig. 8.** Radial buoyant force of the angular element in the circumferential direction (kPa).

the RMS of the mirror deformation. The above three variable parameters are defined as optimization parameters presented below; see Table 1. The equilibrium condition (2) and the range of the optimization parameters are defined as optimization constraints. We employ the Particle Swarm Optimization (PSO) algorithm to find the Pareto optimum in the response function. After a series of iterations, a set of Pareto parameter solutions, minimizing mirror surface deformation with the axis horizontal, are shown in Table 1.
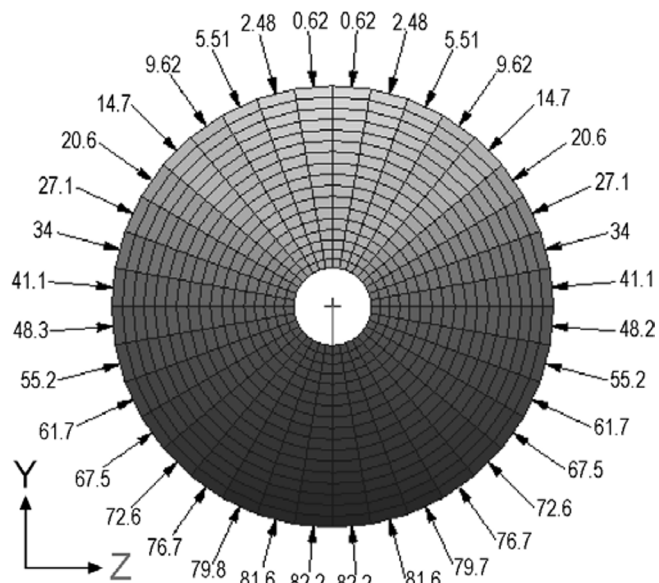
**Table 1.** Optimization Results.

| Variable parameters to be optimized | Parameter value range | Optimum value |
|---|---|---|
| Envelope angle of the mercury tube, $2\theta_{\max}$ | $180° - 360°$ | $180°$ |
| Proportion of the primary mirror's gravity borne by the mercury tube, $P_m$ | $50\% - 100\%$ | $92\%$ |
| Axial distance of the mercury tube from the primary mirror's center of gravity, $D_m$ | $-10 \text{ mm} - 10 \text{ mm}$ | $5 \text{ mm}$ |

### 3.3. Deformation of the Primary Mirror in Variable Orientation

We analyze the deformation of the primary mirror in variable orientation; see Fig. 9.

From the results of the FEA analysis, one can observe that, with the horizontal mirror axis, only the radial forces would act, the deformation contours are mainly distributed in bands at vertical direction, the lower region of the deformation is mainly caused by the mercury tube, and the upper part is caused by the central hub. As the elevation angle of the mirror's axis changes, the proportion of the mirror
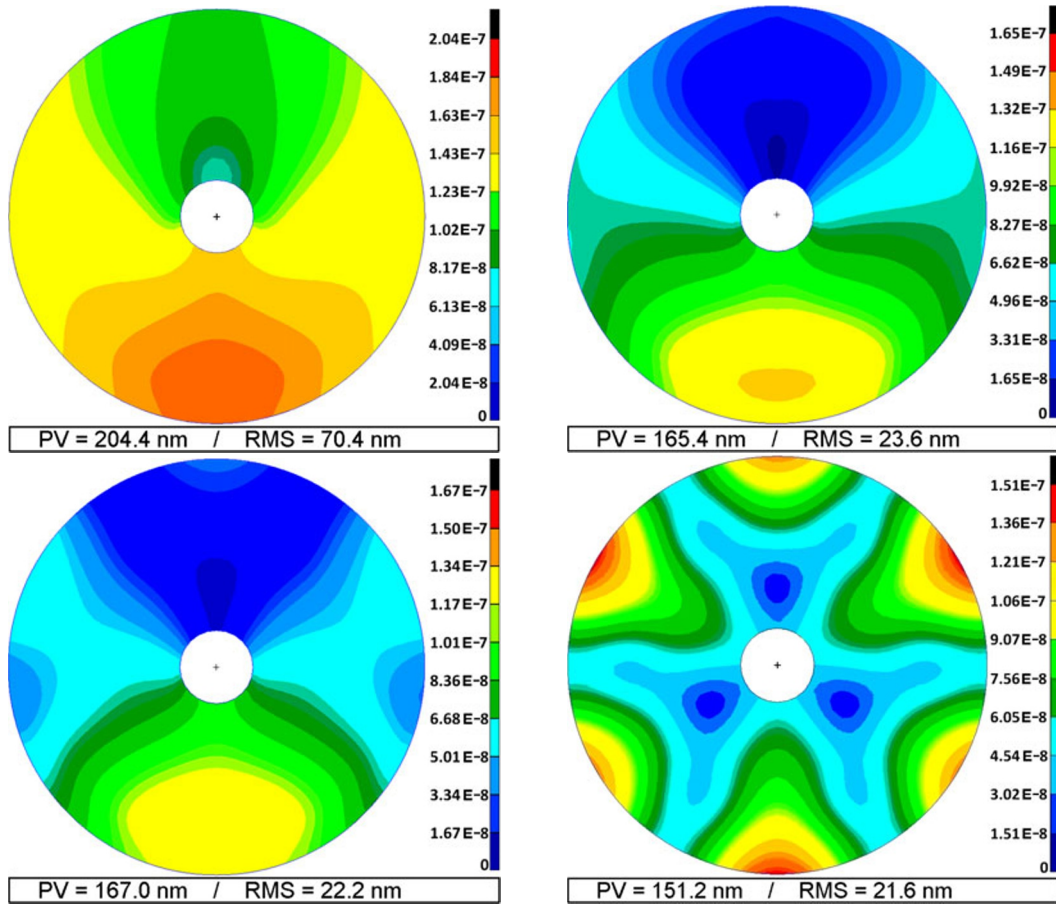
**Fig. 9.** Deformation of the primary mirror in variable orientation horizon (a), 30° (b), 60° (c), and zenith (d).

weight borne by the axial support gradually increases, and the width of the strip deformation band at lower region gradually decreases. As the antenna elevates to zenith, most of the mirror weight is borne by the axial support, and the deformation contours are symmetrically distributed in a ring.

# 4. Evaluation of Low-Order Aberrations over the Primary Mirror Surface Based on Annular Zernike Polynomials

The advantage of the Zernike polynomials is that they are easily related to the classical aberrations and can be fitted to any measured wavefront by best least square fitting. So the suppression effect of the optimized composite mount on the low-order aberration of the primary mirror can be evaluated by the Zernike polynomials [8]. It should be noted that the object studied is a primary mirror with a central hole, resulting in orthogonal failure of classical Zernike polynomials. Therefore, the aberrations are fitted using annular Zernike polynomials, which are a modified set of Zernike polynomials and are orthogonal over an annular aperture.

In the previous section, we obtained the nodal coordinates $G(x_i, y_i, z_i)$ of the primary mirror mirrors and the deformed rigid body displacements $\Delta x_i$, $\Delta y_i$, and $\Delta z_i$, in view of the FEA method. In order to

relate the FEA results to annular Zernike polynomials, first it is necessary to transform the coordinates of the FEA results from the Cartesian coordinate system into the normal coordinate system; see Fig. 10.
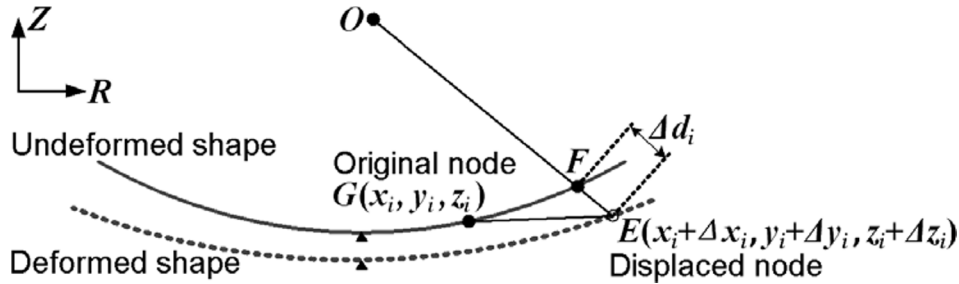


**Fig. 10.** Schematic diagram of the transformation the FEA results into the normal coordinate system.

Here, $R$ and $O$ are the radius and center of the primary mirror, respectively. Due to the mirror deformation, the original node $G(x_i, y_i, z_i)$ on the non-deformed shape moves to $E(x_i + \Delta x_i, y_i + \Delta y_i, z_i + \Delta z_i)$. The intersection of a vertical line through node $E$ to the non-deformed shape is node $F$, the direction of $\overrightarrow{EF}$ is normal, and $\Delta d$ is the length of $\overrightarrow{EF}$ in the normal coordinate system. Note that $|GF|$ is very small, so $\overrightarrow{OG}$ and $\overrightarrow{OF}$ are approximately parallel, then

$$\Delta d = |\overrightarrow{EF}| = \overrightarrow{GE} \cdot \overrightarrow{FO}_{\text{normalization}} = \Delta z - \frac{x\Delta x + y\Delta y + z\Delta z}{R}. \tag{6}$$

Subsequently, the coordinates of the original node $(x_i, y_i)$ are converted to $(\rho_i, \theta_i)$ in the polar coordinate system, and $\rho_i$, $\theta_i$, and $\Delta d_i$ are substituted into the $N$-term annular Zernike polynomials with $N$-term, namely,

$$\begin{cases} c_1 Z_1(\rho_1, \theta_1) + c_2 Z_2(\rho_1, \theta_1) + \cdots + c_n Z_n(\rho_1, \theta_1) = \Delta d_1 \\ c_1 Z_1(\rho_2, \theta_2) + c_2 Z_2(\rho_2, \theta_2) + \cdots + c_n Z_n(\rho_2, \theta_2) = \Delta d_2 \\ \qquad\qquad\qquad\qquad \vdots \\ c_1 Z_1(\rho_m, \theta_m) + c_2 Z_2(\rho_m, \theta_m) + \cdots + c_n Z_n(\rho_m, \theta_m) = \Delta d_m \end{cases}, \tag{7}$$

where $m$ is the count of nodes on the mirror surface.

Each coefficient of the annular Zernike polynomials can be obtained by solving the least squares solution of the hyperstatic equations (7). Then the normal RMS error of mirror surface can be computed, using the following formula:

$$e_{\text{RMS}} = \left\{ \frac{1}{\pi(1 - \varepsilon^2)} \int\limits_0^{2\pi} \int\limits_\varepsilon^1 \Delta s^2(\rho, \theta)\rho \, d\rho \, d\theta - \frac{1}{\pi^2(1 - \varepsilon^2)^2} \left[ \int\limits_0^{2\pi} \int\limits_\varepsilon^1 \Delta s(\rho, \theta)\rho \, d\rho \, d\theta \right]^2 \right\}^{1/2}. \tag{8}$$

The terms include an annulus ratio $\varepsilon$, which is defined as the ratio of the inner annular radius to the outer radius of the aperture. The evaluation process of the low-order surface error performance can be described; see Fig. 11.

The annular Zernike polynomial representation of wavefront errors is convenient for describing traditional low-order aberrations and high spatial frequency defects. In general, 10 terms are amply sufficient to describe wavefront errors due to misalignment, mechanically-induced deformations, and figuring errors
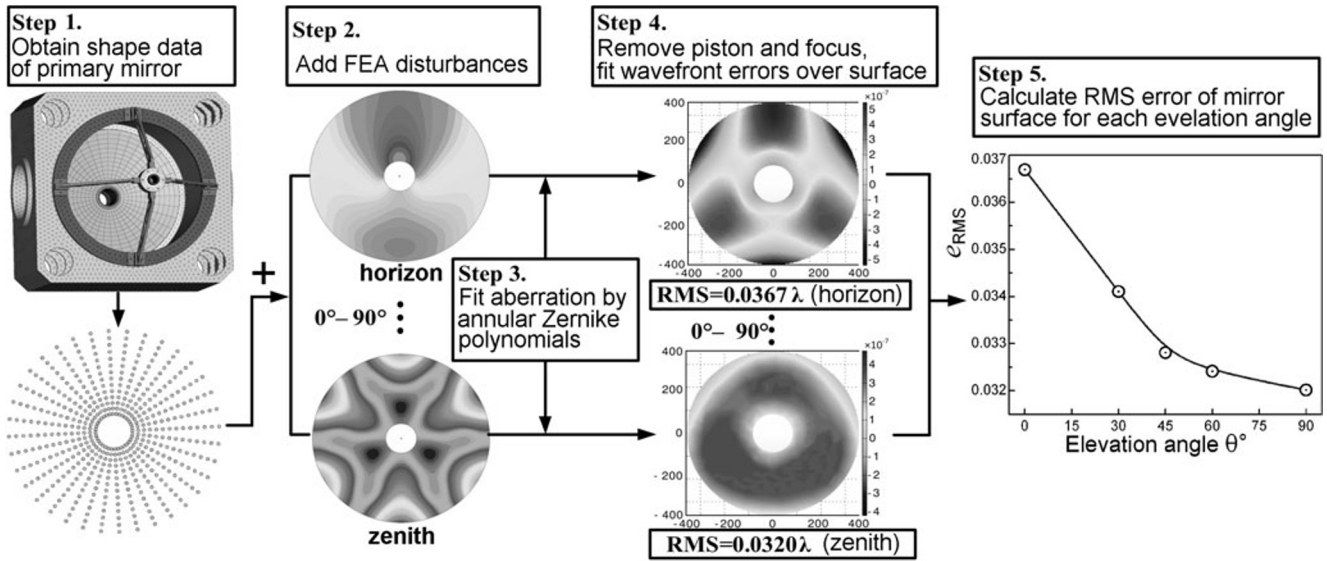
**Fig. 11.** Process and results of low-order surface error evaluation of a mirror surface.

in the optics [9]. By plugging the shape data and the FEA disturbances into Eq. (8), we can establish the relationship between the common low-order aberrations and the initial 10 term coefficients of the annular Zernike polynomials; see Table 2.

**Table 2.** Relationship between Common Low-Order Aberrations and Initial Coefficients of the Annular Zernike Polynomials.

| Low-order aberrations | Zernike polynomial expressions for aberration | Aberration value as the elevation angle $\theta$ of the mirror changes | | | |
|---|---|---|---|---|---|
| | | $\theta = 0°$ (horizontal) | $\theta = 0°$ (before optimiz.) | $\theta = 45°$ | $\theta = 90°$ (vertical) |
| $W_{\text{Astigmatism}}$ | $2\sqrt{(Z_5^2 + Z_6^2)/(1 + \varepsilon^2 + \varepsilon^4)^{1/2}}$ | $1.2054 \cdot 10^{-5}$ | $2.3698 \cdot 10^{-4}$ | $6.6487 \cdot 10^{-6}$ | $4.5376 \cdot 10^{-6}$ |
| $W_{\text{Coma}}$ | $\dfrac{3(1 + \varepsilon^2)(Z_7^2 + Z_8^2)^{1/2}}{(1 - \varepsilon^2)[(1 + \varepsilon^2)(1 + 4\varepsilon^2 + \varepsilon^4)]^{1/2}}$ | $3.3347 \cdot 10^{-6}$ | $6.6598 \cdot 10^{-5}$ | $3.001 \cdot 10^{-6}$ | $2.7410 \cdot 10^{-6}$ |
| $W_{\text{Spherical}}$ | $6Z_9(1 - \varepsilon^2)^{-2}$ | $-7.684 \cdot 10^{-7}$ | $6.4653 \cdot 10^{-6}$ | $-5.663 \cdot 10^{-7}$ | $3.0121 \cdot 10^{-7}$ |

TOGS generally features a focusing unit, so the piston and focus of the aberrations can be ignored. Once the coefficients of the annular Zernike polynomials were calculated, it is possible to fit the deformation of the primary mirror and calculate the RMS error of the surface shape; see Fig. 11. In Table 2 and Fig. 11, one can observe that the optimized composite mount significantly suppresses the low-order aberration of the primary mirror, resulting in the aberrations due to deformation over the entire surface of the primary mirror; all being smaller than $\lambda/27$ as the elevation angle of the mirror axis changes from horizontal to vertical one, and, in particular, the suppression of astigmatism is reduced by almost 20 times compared to the pre-optimization proved to be very significant and effective. It is important to recall, in any discussion of mirror deformation, that there is a factor of 2 between surface and the exit beam, and, traditionally, a system is considered fully qualified, if the RMS wavefront error of the

exit beam is smaller than $\lambda/10$ [10]. Thus, the wavefront error caused by the primary mirror with the composite mount fully satisfies the system requirements.

## 5.    Experiment Results

The best way to characterize the low-order aberrations of the primary mirror with a support structure consists in examining the wavefront error of the assembled primary mirror, using a ZYGO interferometer. In Fig. 12, we show the experimental site and mirror-surface error of the primary mirror, with the composite mount, in the axis-horizontal position and axis-vertical position, respectively.

As shown in Fig. 12, the RMS of the wavefront error over the entire surface of the horizontal and vertical axes mirrors in the contexts of the radial and axial supports are $0.048\lambda$ and $0.044\lambda$, respectively. The RMS error of the wavefront over the primary mirror surface after fabrication is $0.0263\lambda$, and the wavefront errors caused by fabrication imperfections and the deformation are uncorrelated, respectively. Therefore, the standard deviation synthesis equation applies, namely,

$$\sigma_{\text{deformation}} = \sqrt{(\sigma_{\text{experiment}})^2 - (\sigma_{\text{fabricaion}})^2}. \tag{9}$$
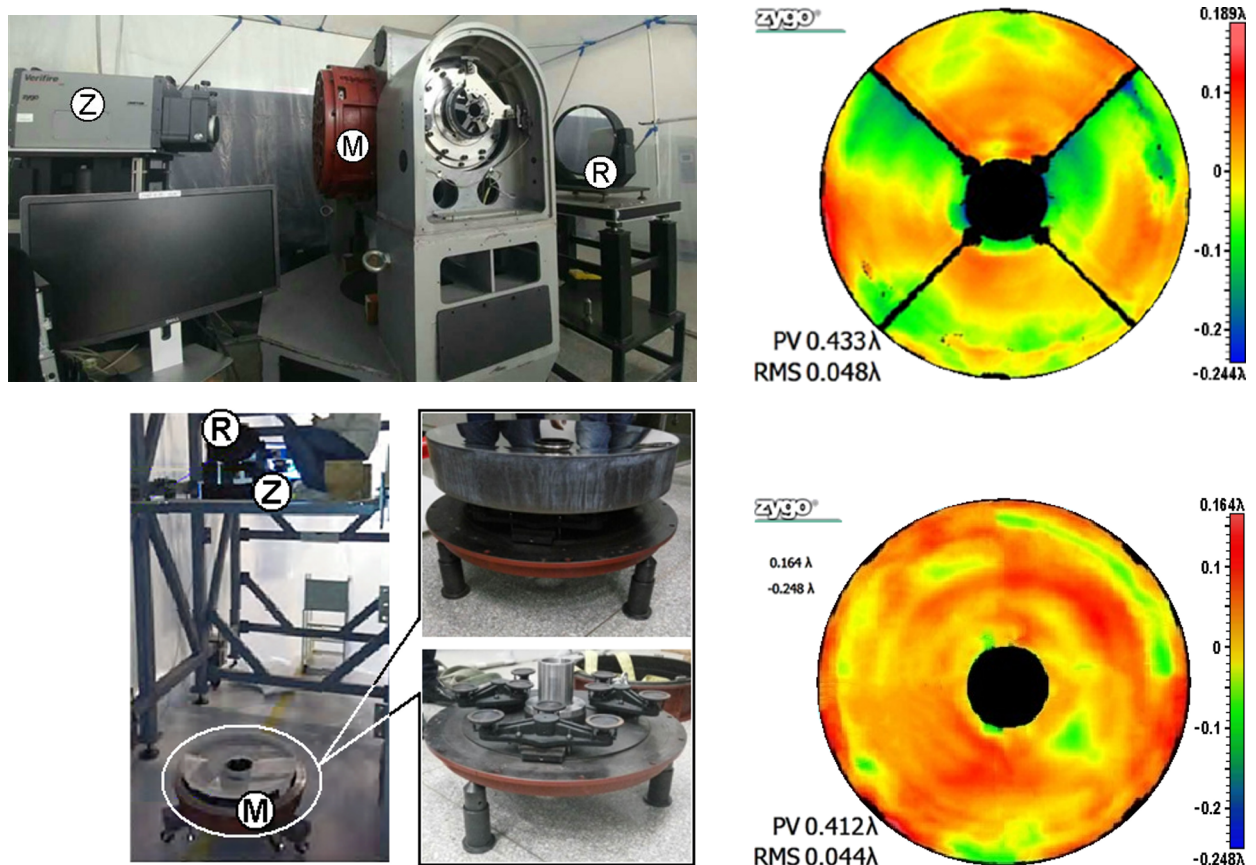


**Fig. 12.** The experimental site (a, c) and mirror-surface error (b, d) of the primary mirror in the axis-horizontal (a, b) and axis-vertical (c, d) positions. Here, $Z$ is the ZYGO interferometer, $M$ is the primary mirror, and $R$ is standard reflector.

Eliminating the fabrication imperfections, the RMS of wavefront error over the entire surface of horizontal and vertical axes mirrors are $0.04\lambda$ and $0.035\lambda$, respectively, and this deformation only results from changing direction of gravity and imperfect support. Compared to the results of the wavefront error fitted by the annular Zernike polynomial; see Fig. 11, the relative wavefront errors are 9.5% and 8.1%, respectively. The relative errors may be attributed to the experimentally detected wavefront and also include misalignment and modeling errors in FEA of the integrated optomechanical analysis. However, the distribution and trend of the two wavefront errors basically match and have basically the same value. Therefore, the above integrated optomechanical analysis results are basically reliable and credible.

## 6. Summary

In this paper, we presented a composite gravity-compensation mount combining a Hindle axial mount, a mercury tube radial mount, and a hub center mount to suppress the low-order aberration of the primary mirror with variable-orientation of a TOGS telescope as it changed pointing. The traditional approach to budgeting wavefront errors is to specify upper limits to the low and high-order aberrations, where low-order aberrations due to misalignment and mechanically-induced deformations are the most difficult to control, while high-order aberrations are easier to be made negligible by proper fabrication or adaptive optics. The low-order aberration suppression technique for the primary mirror based on a composite gravity compensation mount demonstrated in this paper can provide a practical reference for the budget and allocation of the systematic wavefront error in meter-scale optical antenna of the TOGS for satellite downlink.

## Acknowledgments

## References

1. F. Moll, A. Shrestha, and C. Fuchs, et al., *Proc. SPIE*, **9647**, 74 (2015).
2. F. Moll, J. Horwath, and A. Shrestha, et al., *IEEE J. Sel. Areas Commun.*, **33**, 1985 (2015); DOI: 10.1109/JSAC.2015.2433054
3. F. Kurz, D. Rosenbaum, J. Leitloff, et al., "Real time camera system for disaster and traffic monitoring," in: *Proceedings of International Conference on SMPR 2011* (2011), pp. 1–6; `elib.dlr.de/69930/`
4. R. A. Fields, D. A. Kozlowski, H. T. Yura, et al., "5.625 Gbps bidirectional laser communications measurements between the NFIRE satellite and an Optical Ground Station," in: *2011 International Conference on Space Optical Systems and Applications (ICSOS)*, Santa Monica, CA, USA, 2011, pp. 44-53 (2011); DOI: 10.1109/ICSOS.2011.5783708
5. X. Xie, Y. Zhou, S. Yu, et al., *Opt. Commun.*, **463**, 125371 (2020).
6. P. R. Yoder, *Design and Analysis of Large Mirrors and Structures*, CRC Press, New York (2015).
7. A. Luc, *Opt. Eng.*, **34**, 567 (1995).
8. L. Han, C. Liu, C. Fan, et al., *Appl. Opt.*, **57**, 1662 (2018).
9. V. N. Mahajan and J. A. Díaz, *Appl. Opt.*, **52**, 2062 (2013).
10. P. Y. Bely, Ed., *The Design and Construction of Large Optical Telescopes*, Springer, New York (2003).